

Output-Based h - p Refinement Strategy with Anisotropic AMR and High-Order CENO Finite-Volume Scheme for Three-Dimensional Inviscid Flows

C. N. Ngigi and C. P. T. Groth

Corresponding author: chris.ngigi@mail.utoronto.ca

University of Toronto Institute for Aerospace Studies
4925 Dufferin Street, Toronto, Ontario M3H 5T6, Canada

Abstract: The formulation and application a hybrid h - p refinement technique method based on output-based error estimation is considered for the prediction of compressible three-dimensional inviscid flows. The proposed h - p refinement strategy makes use of a block-based anisotropic adaptive mesh refinement scheme (AMR) used in combination with a high-order central essentially non-oscillatory (CENO) finite-volume spatial discretization scheme. The latter achieves high spatial accuracy via cell-centered high-order solution reconstruction. The resulting scheme allows for refinement of the spatial discretization procedure, in which either enhancements of the local mesh spacing, h , or increases in the order of solution reconstruction, p , are allowed to achieve the desired increased solution accuracy. Functional convergence rates and potential benefits of the proposed output-based approach are examined and compared to those of standard gradient-based methods for a candidate compressible inviscid flow problem.

Keywords: Output-Based Error Estimation, Computational Fluid Dynamics.

1 Introduction and Motivation

Numerical simulations that predict complex physical flows having disparate spatial scales are often associated with high computational costs. Two common approaches employed to reduce these costs are high-order spatial discretization methods and adaptive mesh refinement (AMR) techniques. High-order here usually implies that the formal accuracy of the discretization method is greater than second-order accuracy (i.e., $p > 2$, where p denotes the spatial discretization order). The high-order solution accuracy is generally achieved via the evaluation of higher solution derivatives, resulting in lower truncation errors compared to standard lower-order methods. A number of high-order schemes have been developed over the years and these include the Essential Non-Oscillatory (ENO) [1] family of schemes, spectral methods [2, 3, 4], discontinuous Galerkin methods [5, 6, 7], among others. Some of the challenges presented to such high-order schemes is the preservation of solution monotonicity, particularly in the vicinity of large solution gradients or discontinuities as well as under-resolved solution content [8, 9]. Originally proposed by Harten, ENO schemes perform solution reconstruction on multiple stencils and select the smoothest or most monotone stencil among possible candidates. The Weighed ENO (WENO) schemes of Liu *et al.* and extended by others [10, 11, 12] makes use of a weighting procedure for the multiple stencils to reduce computational costs of stencil selection. The central ENO (CENO) finite-volume scheme of Ivan and Groth [8, 9, 13] employs a fixed central stencil and applies a three-step approach. The first step evaluates the K -exact reconstruction of Barth [14] on the single fixed stencil. This is followed by the evaluation of a so-called smoothness indicator. Lastly, in regions deemed non-smooth, the scheme switches to a limited piecewise-linear least squares reconstruction. This effectively preserves solution monotonicity, particularly in the vicinity of shocks and discontinuities, while reducing complexities of ENO and WENO schemes.

AMR techniques [15, 16, 17, 18] are another approach to reducing computational costs and are particularly useful in numerical simulations consisting of disparate spatial scales. This technique evaluates relevant mesh refinement criteria to yield higher local mesh resolution in regions of the computational domain deemed to require higher spatial resolution therefore reducing the overall required mesh size for a given level of solution accuracy. The original parallel block-based AMR techniques proposed by Groth and co-workers [19, 20, 21, 22, 13, 23] group computational cells into blocks and employed physics- or gradient-based mesh refinement strategies that refine or coarsen at block level depending on target thresholds. Such gradient-based techniques have been used in combination with a second-order scheme as well as high-order CENO reconstruction schemes and have been observed to work well for many of the problems studied [24, 25, 26, 27, 28, 29, 30, 13, 23]. However, AMR refinement strategies directed by heuristic physics- or gradient-based criteria can be challenged to efficiently attaining converged solutions of the desired accuracy. For example, for flows involving discontinuities and shocks, such methods can potentially over-emphasize and thus over-refine the non-smooth regions, while for flows that can be characterized as smooth, these refinement strategies do not guarantee error reduction with increased mesh resolution [31, 32]. A more accurate strategy for directing the mesh refinement and thereby reducing solution error is required.

Output-based error estimation methods [33, 31, 34, 35] constitute one approach to addressing the shortcomings of AMR methods identified above. A so-called adjoint or dual problem is solved to provide a measure of the sensitivity of pre-defined engineering functionals of interest to local estimates of the functional error based on the solution residual. The dual and primal solutions are reconstructed on enriched solution spaces to evaluate the error estimates and local error indicators can then be used to flag refinement regions which present the most significant contribution to the defined functional error. As a result, output-based approaches offer more rapid convergence at reduced computational cost compared to physics- and/or gradient-based methods. Various refinement strategies can be deployed, such as mesh (h -) refinement p -based discretization order refinement, as well as combined hybrid or h - p refinement strategies. Babuska and Szabo [36], Oden *et al.* [37], Demkowicz [38], Dolejsi [39, 40] have shown that improved functional error convergence can be obtained by combining h and p refinement methods when compared to pure h -refinement in finite-element methods. Recent work by Jalali and Ollivier-Gooch [41] investigated benefits of h - p adaptation in conjunction with two-dimensional (2D) finite-volume schemes.

2 Scope of Present Study

In the present study, the high-order CENO finite-volume scheme of Ivan and Groth [8, 9, 13, 23] is used along with an output-based error estimation technique for directing hybrid h - p refinement on multi-block, body-fitted, hexahedral meshes for the solution of three-dimensional (3D) inviscid compressible flows. The anisotropic block-based AMR scheme of Freret and Groth [28] and Freret *et al.* [30, 32] is applied herein to allow h -based adaptation of the body-fitted meshes in an anisotropic fashion (i.e., in a preferred coordinate direction). In the high-order CENO spatial discretization scheme, a high-order tricubic representation [42, 43, 32] is used to accurately represent curved boundaries to reduce potential sources of geometrical modelling error. Newton's method is applied to the solution of the coupled non-linear system of algebraic equations resulting from the high-order spatial discretization scheme to obtain converged steady-state solutions to the governing equations on a given computational grid in an efficient manner [30]. The discrete adjoint solution is evaluated at an order of accuracy consistent with the local spatial discretization order, while solution enrichment for error estimate and error indicator evaluation is carried out using a p -based enrichment strategy in terms of a fifth-order ($p = 5$) version of the CENO finite-volume scheme. Venditti and Darmofal [44, 45] among other have previously demonstrated the evaluation of error estimates and error indicators by h refinement, yielding so-called h -derived error estimates and indicators. This approach was successfully applied in the context of the anisotropic block-based AMR considered here for both 3D inviscid and viscous flows by Narechania *et al.* [46] and 3D inviscid flows by Ngigi *et al.* [47]. The h -derived error estimates are obtained by uniformly refining the mesh and coarsening back to the original solution space while the anisotropic error indicators are evaluated by performing anisotropic mesh refinements in each of the three directions. However, Ngigi *et al.* [47] also previously implemented a p -refinement approach to evaluating so-called p -derived error estimates and error indicators for use with the anisotropic block-based AMR scheme of Freret *et al.* [30, 32]. This alternative procedure follows other similar strategies proposed previously by

Yano and Darmofal [48], Ceze and Fidkowski [49], and Wooten *et al.* [50]. The direction for the anisotropic mesh refinement is determined in this case using the anisotropic smoothness indicator of Freret *et al.* [13, 23]. For a number of inviscid flow cases, Ngigi *et al.* [47] observed previously that the proposed p -derived error estimates provide similar performance to the h -derived approach in terms of the resulting adapted meshes and, importantly, yield comparable functional accuracy at a significantly lower overall computational cost. Lastly, in the proposed h - p refinement strategy, a measure based on solution smoothness is used to select between h - and p - refinement: local h -refinement is applied in non-smooth regions while local p -refinement is applied where the solution content is smooth.

In what follows, details of the proposed hybrid h - p refinement method are provided including descriptions of the finite-volume scheme, anisotropic block-based AMR method, and p -driven output-based error estimation procedure. The potential benefits of the proposed output-based approach are examined and compared to those of standard gradient-based methods for a selected compressible inviscid flow problem.

3 High-Order Finite-Volume Scheme

3.1 Governing Equations and Semi-Discrete Formulation

The proposed h - p output-based refinement method is developed here for 3D inviscid compressible flows. The conservative form for the governing equations describing these gaseous flows of interest can be expressed using matrix-vector notation as

$$\frac{\partial \bar{\mathbf{U}}}{\partial t} + \vec{\nabla} \cdot \vec{\mathbf{F}} = \frac{\partial \bar{\mathbf{U}}}{\partial t} + \vec{\nabla} \cdot \vec{\mathbf{F}}_I(\bar{\mathbf{U}}) , \quad (1)$$

where $\bar{\mathbf{U}} = [\rho, \rho u, \rho v, \rho w, e]^T$ is the vector of conserved solution variables which can be expressed in terms of the gas density, components of the velocity vector in the x , y and z directions, and specific total energy denoted by ρ , u , v , w , and e , respectively. Here, $\vec{\mathbf{F}} = \vec{\mathbf{F}}_I$ is the solution flux dyad comprising the so-called hyperbolic or inviscid components of the solution fluxes, $\vec{\mathbf{F}}_I$.

Following application of the integral form of the governing equations in Eq. (1) within a standard finite-volume method to a hexahedral computational cell or element, (i, j, k) , of a structured three-dimensional grid, with Gaussian numerical quadrature rules applied to the evaluation of volume and surface integrals, the following semi-discrete form of the governing equations can be obtained:

$$\begin{aligned} \frac{d\bar{\mathbf{U}}_{ijk}}{dt} &= -\frac{1}{V_{ijk}} \sum_{l=1}^{N_f} \sum_{m=1}^{N_{GF}} \left(\omega_m \left(\vec{\mathbf{F}}_I \right) \cdot \mathbf{n} \Delta \mathcal{A} \right)_{ijk,l,m} \\ &= \bar{\mathbf{R}}_{ijk}(\bar{\mathbf{U}}) , \end{aligned} \quad (2)$$

where N_{GF} is the number of Gauss quadrature points on each of the N_f faces of the cell, ω_m are the quadrature weighting coefficients corresponding to the faces of the cell, $\Delta \mathcal{A}$ denotes the surface area of face l . The residual operator is denoted $\bar{\mathbf{R}}_{ijk}$, V_{ijk} is the volume of the cell (i, j, k) and \mathbf{n} is the normal to the face. The values of the inviscid solution fluxes, $\vec{\mathbf{F}}_I$, at each quadrature point of each face are evaluated here using the HLLC approximate Riemann-solver [51] .

3.2 Newton's Method for Steady Flows

Newton's method is applied to the solution of the coupled non-linear system of algebraic equations that results from the preceding spatial discretization procedures to obtain fully-converged steady-state solutions to the governing equations efficiently. The particular implementation applied here follows the algorithm developed by Groth and co-workers [52, 53, 20] which was extended by Freret *et al.* [30] to the high-order CENO scheme used in conjunctions with anisotropic block-based AMR. The latter is well adapted for computations on large multiprocessor parallel clusters.

For steady-state problems, the semi-discrete form of the governing equations given in Eq. 2 reduces to

$$\frac{d\bar{\mathbf{U}}}{dt} = \mathbf{R}(\bar{\mathbf{U}}) = 0. \quad (3)$$

The solution of this coupled system of non-linear algebraic equations defined by Eq. (3) is then obtained via Newton's method by iteratively solving a sequence of linear systems solved using the iterative generalized minimal residual (GMRES) algorithm of Saad and co-workers [54]. Convergence of the GMRES algorithm is improved by using an additive Schwarz global preconditioner and a block incomplete lower-upper local preconditioner. Refer to the paper by Freret *et al.* [30] for further details.

3.3 Central Essentially Non-Oscillatory (CENO) Finite-Volume Scheme

The high-order CENO finite-volume method of Ivan and Groth [55] and Freret *et al.* [13] uses a single central stencil and thereby affords high-order accuracy at relatively lower computational cost, in contrast to other ENO schemes [56, 10].

3.3.1 K -exact Least Squares Reconstruction

Based on the central stencil, the K -exact least-squares reconstruction [57] of any scalar solution quantity, U_{ijk} , within a cell with index (i, j, k) about the cell-centroid $(x_{ijk}, y_{ijk}, z_{ijk})$ can be expressed as

$$U_{ijk}^K(q, r, s) = \sum_{\substack{p_1=0 \\ p_1+p_2+p_3 \leq K}}^K \sum_{p_2=0}^K \sum_{p_3=0}^K (q - x_{ijk})^{p_1} (r - y_{ijk})^{p_2} (s - z_{ijk})^{p_3} D_{p_1 p_2 p_3} . \quad (4)$$

The constant coefficients, $D_{p_1 p_2 p_3}$, of the reconstruction polynomial are referred to as the unknown derivatives which are evaluated via the least-squares solution of an overdetermined system of linear equations given by

$$\mathbf{A}\mathbf{x} - \mathbf{c} = \mathbf{e}, \quad (5)$$

where \mathbf{A} is a coefficient matrix dependent on the reconstruction stencil geometry, \mathbf{c} is a vector containing the average solution data at each time step, and \mathbf{e} is the the mean value error in each control volume. The coefficients $D_{p_1 p_2 p_3}$ are contained in the solution vector, \mathbf{x} .

Singular value orthogonal decomposition (SVD) is used to solve the weighted least-squares problem associated with the CENO reconstruction [58]. This approach permits the computation of a pseudo-inverse matrix after which the solution of the least-squares problem is given by a simple matrix-vector product. The use of a single fixed central reconstruction stencil, affords the storage and re-use of a pseudo-inverse matrix for the reconstruction of all variables. The resulting overdetermined system provides the values of the Taylor derivatives, $D_{p_1 p_2 p_3}$, which define the unlimited high-order reconstruction polynomial.

3.3.2 Smoothness Indicator and Monotonicity Enforcement

The CENO finite-volume scheme ensures monotonicity by evaluating a solution smoothness indicator as described by Ivan et al [58]. It is computed as follows

$$\mathcal{S} = \frac{\alpha}{\max(1 - \alpha, \epsilon)} \frac{\mathcal{N}_{\text{SOS}} - \mathcal{N}_D}{\mathcal{N}_D - 1}, \quad (6)$$

where \mathcal{N}_{SOS} is an integer value representing the size of stencil, \mathcal{N}_D represents the degrees of freedom (the number of unknowns) in the K -exact polynomial reconstruction, ϵ is a value to avoid division by zero, and α is the smoothness parameter. The value of α for cell (i, j, k) and solution variable u has the form

$$\alpha = 1 - \frac{\sum_{\gamma} \sum_{\delta} \sum_{\zeta} (u_{\gamma\delta\zeta}^K(\vec{X}_{\gamma\delta\zeta}) - u_{ijk}^K(\vec{X}_{\gamma\delta\zeta}))^2}{\sum_{\gamma} \sum_{\delta} \sum_{\zeta} (u_{\gamma\delta\zeta}^K(\vec{X}_{\gamma\delta\zeta}) - \bar{u}_{ijk})^2}, \quad (7)$$

where the indices $(\gamma\delta\zeta)$ represent the elements of the supporting reconstruction stencil for the cell (i, j, k) , $u_{\gamma\delta\zeta}^K(\vec{X}_{\gamma\delta\zeta})$ is the reconstruction polynomial belonging to cell (γ, δ, ζ) evaluated at the cell center of cell

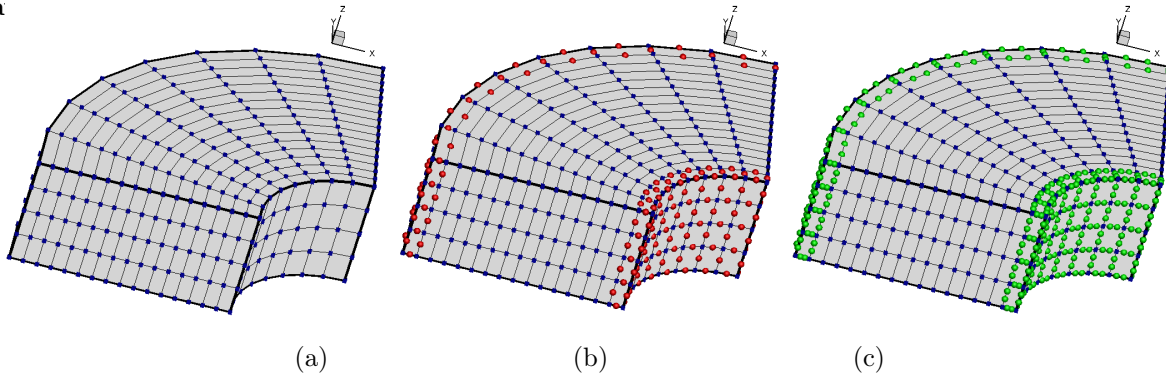


Figure 1: High-order geometry representation using serendipity-type shape functions. (a) Trilinear mapping involves one shape function per node, resulting in 8 shape functions per cell. (b) Hybrid triquadratic mapping where only boundary-adjacent cells have one additional node (depicted in cyan) per cell edge. (c) Hybrid tricubic mapping inserts two nodes (depicted in green) per cell edge having 32 shape functions per cell.

(γ, δ, ζ) , $u_{ijk}^K(\vec{X}_{\gamma\delta\zeta})$ is the extrapolated value of the reconstruction polynomial of cell (i, j, k) obtained by extending $U_{ijk}^k(x, y, z)$ out to the cell center of (γ, δ, ζ) . \bar{u}_{ijk} is the average value of cell (i, j, k) .

Based on the magnitude relative to a chosen cut-off value, \mathcal{S}_C , a large value of \mathcal{S} indicates smooth variations while a small value of \mathcal{S} indicates non-smooth or under-resolved solution content. In the case of the latter, the CENO scheme switches to a limited piecewise-linear least squares reconstruction to ensure solution monotonicity. In this study, the cut-off value of the smoothness indicator cut-off value is taken to be $\mathcal{S}_C = 1,500$ and the Venkatakrishnan limiter [59] is used in conjunction with linear least-squares reconstruction to ensure solution monotonicity.

3.4 High-Order Geometry Representation

Typical flow problems of interest in computational fluid dynamics (CFD) can involve domains with curved boundaries consisting of non-planar computational cells. Accurate representation of such geometries is required for the correct and consistent evaluation of mesh quantities, such as the positions of volumetric and face Gauss integration points used for to determine properties such as cell volumes, face areas, moments, and centroid positions. This in turn facilitates more accurate enforcement of boundary conditions and the evaluation of numerical fluxes and source terms. Representation of such boundaries must be consistent with the spatial discretization order of the underlying scheme to reduce potential geometrical modeling error. Such errors would otherwise dominate the numerical error term to effectively reduce the accuracy of the numerical results.

Serendipity-type shape functions can be used to map the geometrical properties of the computational cells in the physical space to a regular Cartesian space [43, 42] in which the reference hexahedral element [43] defines shape functions at prescribed node positions within the domain. Similar approaches have been adopted in other high-order finite-volume schemes of Ollivier-Gooch *et al.* [60, 61], Costa *et al.* [62] and Freret *et al.* [32]. For trilinear representations, shape functions are defined only on the element vertices as illustrated in Figure 1(a). The triquadratic mapping of Figure 1(b) inserts an additional node at the middle of each edge for a total of 20 shape functions per cell, while the tricubic mappings of Figure 1(c) adds two additional nodes along each edge for a total of 32 shape functions per cell. Freret *et al.* [32] demonstrated triquadratic and tricubic formulations to achieve 4th-order accurate geometry representation.

In this work, a hybrid mapping approach based on the serendipity-type shape functions has been adopted. This consists of a tricubic mapping for the boundary-adjacent cells (those adjacent to curved boundaries) and a trilinear mapping for the cells that are not adjacent to the boundaries. This hybrid approach achieves high-order accurate geometry description while reducing the associated computational costs of achieving high-order accuracy.

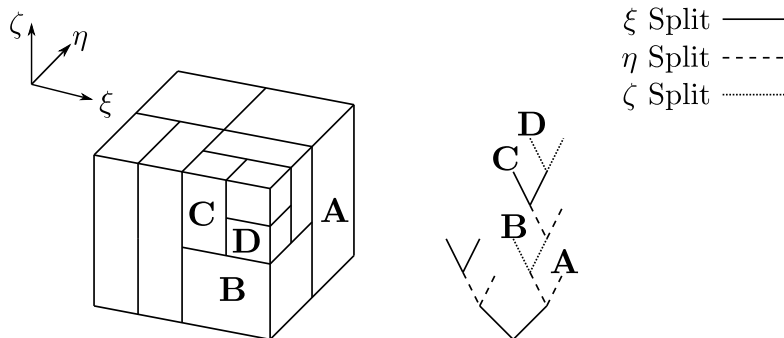


Figure 2: 3D binary tree and the corresponding blocks after several refinements

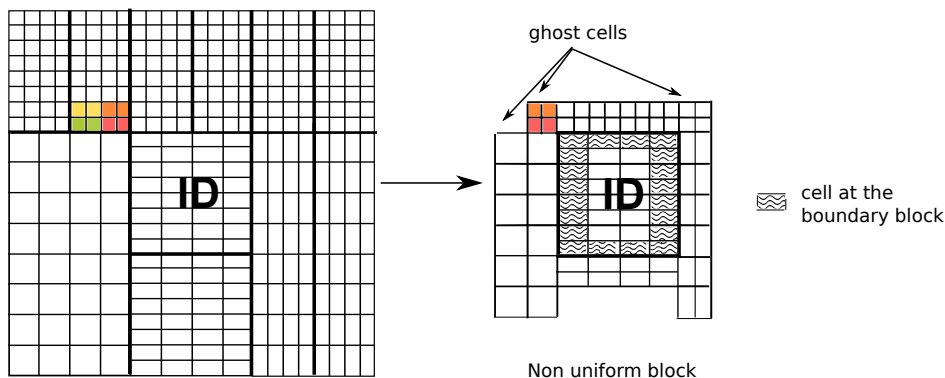


Figure 3: Example of non-uniform block showing solution content and mesh refinement level storage of adjacent neighbour blocks.

4 Anisotropic Block-Based Adaptive Mesh Refinement

AMR allows for localized grid resolution to improve solution accuracy at a lower cost. The block-based AMR approach as developed by Groth and co-workers [24, 63, 29, 64, 27, 26, 22] is applicable to body-fitted multiblock grids. Computational cells are grouped into blocks with mesh refinement being performed at block level and this readily facilitates parallel implementation of finite-volume solution methods for the solution of a range of flow problems, including the modelling of reactive flows [29, 65, 66, 64]. For the anisotropic extension of this approach of Freret *et al.* [30, 23], a hierarchical binary tree, as depicted in Figure 2, is used to track grid refinement in preferred directions as dictated by appropriate refinement criteria. This hierarchical data structure is used to track unstructured grid block connectivity and is generally lighter than conventional unstructured meshing techniques, having lower information storage requirements. Ghost cells lying on the periphery of the grid blocks are stored in so-called non-uniform block structures [22, 30, 23], which contain directly both the solution content and mesh information associated with adjacent neighbour blocks, which may be at different levels of refinement. The non-uniform block approach readily enables anisotropic refinement of the multi-block grid, eliminates the need for solution flux corrections and the prolongation and restriction of solution content otherwise required at block interfaces with grid resolution changes, and generally simplifies the parallel implementation of the AMR procedure, particularly for high-order spatial discretization.

5 Output-Based Error Estimation

In the output-based error estimation approach developed and applied herein, the primal solution to the steady-state governing equations is required for a given computational grid along with the evaluation of a specified functional of interest for the given mesh. A linear system of equations is then established from the definition of the steady-state solution residual and its Jacobian which relates the derivatives of the functional to the discrete adjoint (dual variables). The discrete adjoint provides a measure of sensitivity of the functional to perturbations in the solution residual. The primal and dual solutions are then enriched via solution reconstruction using the CENO finite-volume scheme at order ($K = 4$) to obtain an estimate of the functional error as well as evaluate local error indicators that are then used to flag locally grid blocks for refinement. In this study, the smoothness indicator as described in Section 3.3.2 is used to identify smooth regions within the flagged blocks. Flagged solution/grid blocks deemed smooth are marked for p -refinement while those containing non-smooth content are flagged for h -refinement.

5.1 Discrete Adjoint Equation

Given a coarse mesh, H , and spatial discretization order, \mathcal{P} , the primal solution $\mathbf{U}_{H,\mathcal{P}}$ on the coarse space, $\Omega_{H,\mathcal{P}}$, is required, where the parameter, \mathcal{P} , refers to the order of the spatial discretization scheme, and H describes the resolution level of the given computational grid. The solution on the coarse mesh, H , with resolution, \mathcal{P} , and denoted by $\mathbf{U}_{H,\mathcal{P}}$ is obtained by solving Eq. (1) which are expressed in a semi-discrete form within the finite-volume method as

$$\frac{d\mathbf{U}_{H,\mathcal{P}}}{dt} = \mathbf{R}_{H,\mathcal{P}}(\mathbf{U}_{H,\mathcal{P}}) = 0 \quad (8)$$

An engineering quantity of interest, J , which can be expressed as $J = J(\mathbf{U}_{H,\mathcal{P}})$ is evaluated based on solution $\mathbf{U}_{H,\mathcal{P}}$. A discrete adjoint problem can then be defined as

$$\left[\frac{\partial \mathbf{R}_{H,\mathcal{P}}}{\partial \mathbf{U}_{H,\mathcal{P}}} \right]^T \Psi_{H,\mathcal{P}} = \left(\frac{\partial J_{H,\mathcal{P}}}{\partial \mathbf{U}_{H,\mathcal{P}}} \right)^T. \quad (9)$$

where $\Psi_{H,\mathcal{P}}$ is the solution to the discrete adjoint equation, $(\partial J_{H,\mathcal{P}}/\partial \mathbf{U}_{H,\mathcal{P}})$ is the functional derivative, and $\mathbf{R}_{H,\mathcal{P}}(\mathbf{U}_{H,\mathcal{P}})$ is the primal solution residual. The residual Jacobian can be expressed as

$$\frac{\partial \mathbf{R}_{i,j,k}}{\partial \bar{\mathbf{U}}_J} = -\frac{1}{V_{i,j,k}} \sum_{l=1}^{N_f} \sum_{m=1}^{N_{GF}} \left[\left(\mathbf{A}^{-1} \frac{\partial \vec{\mathbf{F}}_I}{\partial \bar{\mathbf{U}}_J} \mathbf{A} \right) \Delta \mathcal{A} \right]_{i,j,k}, \quad (10)$$

where $\bar{\mathbf{U}}_J$ refers to the cell-average solution in cell J in the reconstruction stencil of cell (i, j, k) , \mathbf{A} is a rotation matrix that rotates only the momentum vector to a local coordinate direction aligned with the outward normal of the cell face, leaving the mass and energy fluxes unchanged, N_{GF} represents the number of Gauss quadrature points on the face f , and $\Delta \mathcal{A}$ is the face area.

Care must be taken to ensure the the evaluation of the adjoint variables is at an order of accuracy matching that of the underlying spatial discretization scheme to facilitate accurate evaluation of error estimates. In this study, the adjoint evaluation is based on the full non-linearized Jacobian residual that is consistent with the order of the underlying spatial discretization scheme. Two key steps are important for this. First, the left and right solution states must be reconstructed to an order of accuracy matching that of the underlying spatial discretization scheme, and, second, the contributions of solution content associated with elements in the reconstruction stencil must be accounted for. For this, the hyperbolic flux component, \mathbf{F}_I , can be expressed as a function of the conserved solution variables to the left (interior) and right (exterior) of a cell face

$$\vec{\mathbf{F}}_I = \vec{\mathbf{F}}_I(\vec{\mathbf{U}}_L, \vec{\mathbf{U}}_R), \quad (11)$$

and the hyperbolic flux Jacobian can then be written as follows

$$\frac{\partial \bar{\mathbf{F}}_I}{\partial \bar{\mathbf{U}}_J} = \left(\frac{\partial \bar{\mathbf{F}}_I}{\partial \mathbf{U}_L} \right) \left(\frac{\partial \mathbf{U}_L}{\partial \bar{\mathbf{U}}_J} \right) + \left(\frac{\partial \bar{\mathbf{F}}_I}{\partial \mathbf{U}_R} \right) \left(\frac{\partial \mathbf{U}_R}{\partial \bar{\mathbf{U}}_J} \right), \quad (12)$$

where \mathbf{U}_L is the reconstructed solution value at the quadrature point on the left side of the cell interface, \mathbf{U}_R is the reconstructed solution value to the right of the cell interface, $\partial \bar{\mathbf{F}}_I / \partial \mathbf{U}_L$ is the flux Jacobian with respect to the reconstructed left solution value, $\partial \bar{\mathbf{F}}_I / \partial \mathbf{U}_R$ is the flux Jacobian with respect to the reconstructed right solution value, $\bar{\mathbf{U}}_J$ is the cell average reconstruction stencil member J , $\partial \mathbf{U}_L / \partial \bar{\mathbf{U}}_J$ is the reconstructed left state Jacobian with respect to $\bar{\mathbf{U}}_J$, and $\partial \mathbf{U}_R / \partial \bar{\mathbf{U}}_J$ is the reconstructed right state Jacobian with respect to $\bar{\mathbf{U}}_J$. The flux and solution vector Jacobians needed to form the adjoint matrix system are evaluated using the Adept automated differentiation (AD) software library of Hogan [67].

Once the residual Jacobian, $\partial \mathbf{R}_{H,p} / \partial \mathbf{U}_{H,p}$, and functional derivative with respect to the conserved variables, $\partial J_{H,p} / \partial \mathbf{U}_{H,p}$, have been constructed, the linear system of Eq (9) is solved using a GMRES solver from the Trilinos software library [68].

5.2 Evaluation of p -derived Error Estimates and Indicators for Directing Anisotropic AMR

As mentioned previously, p -derived error estimates and indicators are used herein for directing the anisotropic AMR. In particular, the fifth-order version of the CENO finite-volume scheme is used as the fine-space residual operator to obtain the error estimates which are then used to flag regions in the computational domain for refinement or coarsening based on specified thresholds. The functional error, δJ , is given by

$$\delta J = J_{H,p}(\mathbf{U}_{H,p}^P) - J_{H,p}(\mathbf{U}_{H,p}), \quad (13)$$

where $\mathbf{U}_{H,p}^P$ and $\mathbf{U}_{H,p}$ are the reconstructed and fine space primal solution vectors, respectively, $J_{H,p}(\mathbf{U}_{H,p}^P)$ is the reconstructed functional on the finer computational space, $\Omega_{H,p}^P$, and $J_{H,p}(\mathbf{U}_{H,p})$ is the exact fine space value of the functional. As the direct evaluation of the latter is undesirable due to the higher evaluation cost, the functional error is instead approximated [69] as follows

$$\delta J \approx \underbrace{(\boldsymbol{\Psi}_{H,p}^P)^T \mathbf{R}_{H,p}(\mathbf{U}_{H,p}^P)}_{\text{computable correction}} + \underbrace{(\mathbf{R}_{H,p}^{\Psi}(\boldsymbol{\Psi}_{H,p}^P))^T (\mathbf{U}_{H,p} - \mathbf{U}_{H,p}^P)}_{\text{error in computable correction}}, \quad (14)$$

where $\boldsymbol{\Psi}_{H,p}^P$ is the reconstructed discrete adjoint solution, $\mathbf{R}_{H,p}(\mathbf{U}_{H,p}^P)$ is the reconstructed primal solution residual. The dot product of these two terms is called the computable correction. The error in the computable correction is given by the inner product of the reconstructed adjoint residual, $\mathbf{R}_{H,p}^{\Psi}(\boldsymbol{\Psi}_{H,p}^P)$, and a vector defined as the difference in the exact fine-space and reconstructed primal solution.

The error indicator in this work is based on the error in the computable correction (ECC) as described by Becker and Rannacher [70] and Venditti and Darmofal [34] that combines the contributions of the adjoint and primal residuals. Giles and Pierce [31] have shown that the ECC form leads to greater functional accuracy by factoring in both the primal and adjoint solution residuals. The p -derived ECC error indicator is thus evaluated here as

$$\mathcal{E}_{K_{H,p}} = \frac{1}{2} \left[\left| \left[\boldsymbol{\Psi}_{H,p}^P - \boldsymbol{\Psi}_{H,p} \right] \left[\mathbf{R}_{H,p}(\mathbf{U}_{H,p}^P) \right] \right| + \left| \left[\mathbf{U}_{H,p}^P - \mathbf{U}_{H,p} \right] \left[\mathbf{R}_{H,p}^{\Psi}(\boldsymbol{\Psi}_{H,p}^P) \right] \right| \right]. \quad (15)$$

Since the local error indicators are evaluated on a cell basis, blocks are flagged for refinement or coarsening based on maximum values for all the cells they contain.

5.3 Refinement Strategies

The output-based error estimates of the previous section are subsequently used to flag those regions of the computational domain that are contributing significantly to the numerical error in the predicted functional

value. Reducing the numerical error in these regions is necessary to realize the benefits of the output-based error refinement technique. The three possible adaptive strategies based on the error estimates will be considered here for reducing the overall estimated error in the functional:

1. ***h*-refinement**: The mesh resolution is modified locally. Since the effective mesh spacing is locally reduced, the discretized form of the governing equations approach their continuous form, and numerical accuracy is improved.
2. ***p*-refinement**: The underlying order of the spatial discretization scheme is modified locally. In this process higher-order spatial derivatives are calculated and used to evaluate more accurate reconstructed solution values in the evaluation of inviscid and viscous fluxes at the cell interfaces. As indicated in Section 3.3, a means of ensuring solution monotonicity must be implemented, as has been done in the CENO finite-volume method of Ivan and Groth [71] and extended by Freret *et al* [30]. As described by researchers as Yano *et al* [72], Ceze and Fidkowski [73] among many others, the benefits of a *p*-refinement approach depends on the availability of an optimal mesh such that features which can prevent the formal achievement of high-order accuracy are avoided. Thus, *p*-refinement is often required to work in tandem with *h*-refinement to realize the full benefits of the approach for many practical applications.
3. **Hybrid *h-p* refinement**: A combined approach in which the mesh is flagged for refinement in non-smooth regions and flagged for *p*-refinement where the flow is smooth. As has been mentioned for the *p*-refinement approach, it is important to identify regions that are under-resolved, non-smooth, or have discontinuities. Hybrid *h-p* approaches have been considered in discontinuous Galerkin and finite-element methods by researchers such as Babuska and Szabo [36], Oden *et al.* [37], Demkowicz [38], Dolejsi [39, 40], Yano *et. al* [72], and Ceze and Fidkowski [73] among many others. Such an approach has also been recently considered for 2D finite-volume schemes by Jalali and Ollivier-Gooch [41].

5.4 Anisotropy Detection for Mesh Refinement

As the local *p*-derived error estimates are isotropic in nature, in order to perform anisotropic mesh refinement using *p*-derived error estimates and criteria, there is need for a measure of directional preference that may exist due to features of the flow physics. Various methods that measure directional bias in the flow quantities can be used for this purpose. For example, a Hessian-based strategy similar to the strategies previously considered by Peraire *et al.* [74], Venditti and Darmofal [44], and Fidkowski and Darmofal [75] can be used. This involves the evaluation of the Hessian of a suitable scalar (such as the Mach number). The principle directions of the largest eigenvalues of the Hessian are then used to determine preferential refinement directions.

In this work, the anisotropic smoothness indicator \mathcal{S}_γ of Freret *et al.* [30, 23] following from Eq. (6) is instead used to detect anisotropic features and flag blocks for refinement in the preferred logical coordinate directions. This anisotropic smoothness indicator takes the form

$$\mathcal{S}_\gamma = \frac{\alpha_\gamma}{\max((1 - \alpha_\gamma), \epsilon)} \quad (16)$$

where α_γ is determined as follows

$$\alpha_\gamma = 1 - \frac{\sum_{\delta} \sum_{\xi} (u_{\gamma, \delta, \xi}^K(\vec{r}_{\gamma, \delta, \xi}) - u_{i, j, k}^K(\vec{r}_{\gamma, \delta, \xi}))^2}{\sum_{\delta} \sum_{\xi} (u_{\gamma, \delta, \xi}^K(\vec{r}_{\gamma, \delta, \xi}) - \bar{u}_{i, j, k})^2}, \quad (17)$$

where $u_{\gamma, \delta, \xi}^K(\vec{r}_{\gamma, \delta, \xi})$ is the reconstructed solution of cell (γ, δ, ξ) evaluated at $\vec{r}_{\gamma, \delta, \xi}$, $u_{i, j, k}^K(\vec{r}_{\gamma, \delta, \xi})$ is the reconstructed solution of cell (i, j, k) evaluated at $\vec{r}_{\gamma, \delta, \xi}$, and $\bar{u}_{i, j, k}$ is the average solution of cell (i, j, k) . The evaluation of \mathcal{S}_γ is restricted through α_γ to the neighboring cells aligned with the computational cell, (i, j, k) , in the γ direction, thus providing a smoothness indicator for that particular direction only. Depending on a specified smooth/non-smooth cutoff value, \mathcal{S}_c , the solution may then be flagged as smooth for values greater

than \mathcal{S}_c , and non-smooth for values less than \mathcal{S}_c . The coordinate direction having the largest measure of non-smoothness determines the preferred direction for refinement. In this study, values of $\mathcal{S}_c = 2,500$ and $\epsilon = 10^{-3}$ were used.

6 Numerical Results for Transonic Ringleb Flow

The Ringleb flow is a steady, isentropic, compressible, and irrotational flow associated with expanding flow between two streamlines. The resulting flow field is smooth and continuous and analytical solutions can be found for a range of conditions [76, 77]. For this reason, Ringleb flow is a suitable test case to verify the accuracy and convergence rates of spatial discretization schemes applied to the solution of the Euler equations governing inviscid compressible gaseous flows. A transonic variant of Ringleb’s flow has been chosen for this study. The computational domain is defined by the streamlines that correspond to $k_{min} = 0.5$ and $k_{max} = 1.2$ for the lower and upper streamline boundaries. Subsonic inflow is imposed at the upper inflow boundary of the Ringleb streamtube for which $q = 0.3$ and the outflow from the domain is supersonic. To avoid issues with the application of boundary conditions, the exact boundary values obtained from the available analytical solutions are imposed along all of the boundaries of the Ringleb flow domain. While the flow is two-dimensional, 3D solutions for this case can be obtained by extruding the computational domain in the third z -direction and applying inlet and boundary conditions set such that the flow remains two-dimensional.

6.1 Accuracy Assessment for Primal Solution Error

As an initial step, an accuracy assessment was performed to verify the convergence behavior of the \mathcal{L}_1 error norm in the predicted pressure obtained when using both the standard second-order limited piecewise least-squares reconstruction and high-order CENO finite-volume schemes applied to the Ringleb flow of interest. Steady-state solutions were computed on a sequence of six uniformly refined meshes, i.e., meshes consisting of 1, 4, 16, 64, 256 and 1,024 grid blocks, with each block containing $8 \times 8 \times 4 (= 256)$ cells. For the converged solution, the error norm in pressure was evaluated using the expression

$$\mathcal{L}_{1v} = \frac{1}{V_T} \sum_{i,j,k} \iiint_{V_{i,j,k}} \left| p_{i,j,k}^K(x, y, z) - p_{exact}(x, y, z) \right| dv, \quad (18)$$

where $p_{i,j,k}^K(x, y, z)$ is the K -exact reconstruction of the pressure variable evaluated at a position (x, y, z) , and $p_{exact}(x, y, z)$ is the analytical value of the pressure at the same point.

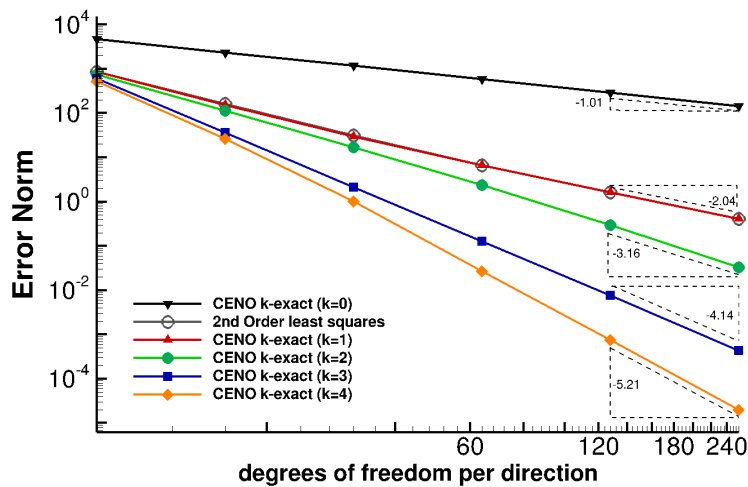


Figure 4: Comparison of pressure error norm convergence for 2^{nd} order least-squares and CENO finite-volume schemes of order $\mathcal{P} = \{1, 2, 3, 4, 5\}$.

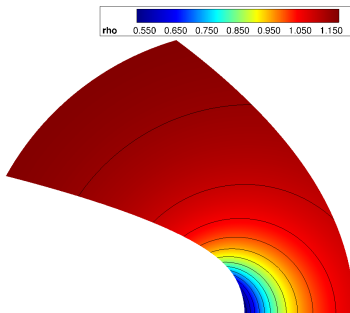


Figure 5: Density contours on final mesh after 5 uniform refinements resulting in 1,024 blocks (262,144 cells).

Figure 4 depicts the resulting convergence rates of the \mathcal{L}_1 pressure error norm. The convergence results depicted in the figure confirm that the limited piecewise linear least squares reconstruction scheme achieves second-order accuracy, while the high-order CENO finite-volume scheme provides an order of spatial accuracy equal to $K+1$, as expected. Additionally, Figure 5 depicts the predicted density contours obtained after 5 uniform refinements resulting in 1,024 blocks (262,144 cells). It is worth noting that the pressure error norm in the case of CENO $K = 4$ is $\approx 10^{-5}$ while that for the $K = 0$ scheme is $\approx 10^3$. The final pressure error norm for the second-order reconstruction scheme is ≈ 1 . Moreover, the convergence order is recovered for fifth-order CENO scheme, which is used in the evaluation of the p -derived error estimates and error indicators in the proposed output-based refinement approach.

6.2 Uniform and Adaptive h -Refinement

The proposed output-based strategy based on the CENO finite-volume scheme was then first applied to the transonic Ringleb flow problem by considering mesh refinement alone for varying orders of spatial discretization, $\mathcal{P} = \{1, 2, 3, 4\}$. Straightforward uniform refinement, gradient-based AMR, and output-based AMR approaches were all considered in the case with the uniform refinement approach serving as a reference baseline result.

For this study, the functional of interest was defined as the absolute error in the pressure evaluated along

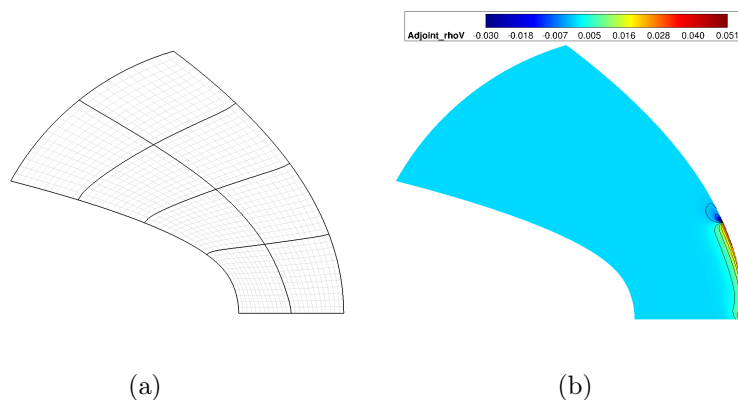


Figure 6: Initial mesh and selected solution contours. (a) Initial mesh consisting of 8 blocks (4,608 cells). (c) y -momentum adjoint contours on final uniform mesh containing 2,048 blocks (1,179,648 cells).

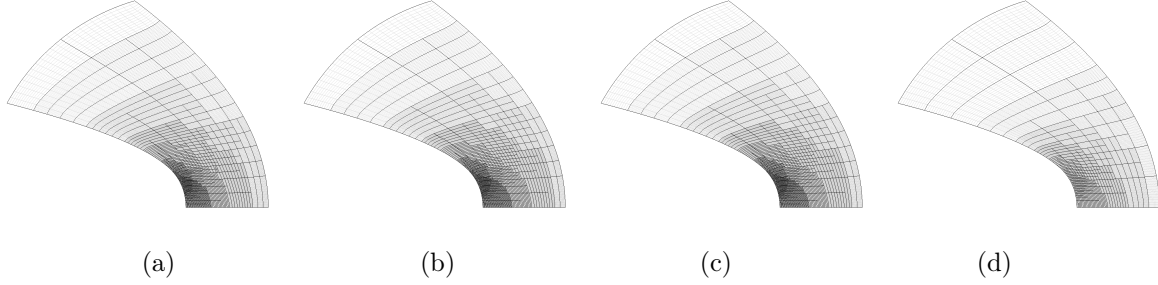


Figure 7: Final meshes obtained using gradient-based refinement strategies for various discretization orders.
(a) Using first-order CENO ($\mathcal{P} = 1$). After 6 refinements, the mesh has 1,412 blocks (813,312 cells), actual error of 1.45×10^0 , and error estimate of 3.39×10^{-1} .
(b) Using second-order CENO ($\mathcal{P} = 2$). After 6 refinements, the mesh has 1,600 blocks (921,600 cells), actual error of 4.95×10^{-3} , and error estimate of 5.65×10^{-4} .
(c) Using third-order CENO ($\mathcal{P} = 3$). After 6 refinements, the mesh has 1,600 blocks (813,312 cells), actual error of 1.78×10^{-3} , and error estimate of 5.13×10^{-4} .
(d) Using fourth-order CENO ($\mathcal{P} = 4$). After 5 refinements, the mesh has 459 blocks (264,384 cells), actual error of 9.14×10^{-5} , and error estimate of 1.08×10^{-5} .

the outer streamline boundary of the Ringleb flow for values of y in the range of $0 \leq y \leq 2$ as follows

$$J(\mathbf{U}) = \frac{1}{A_T} \iint \left| p_a - p_e \right| da, \quad (19)$$

where A_T refers to the cell face area within the specified y range on the outer boundary, p_a is the predicted pressure, p_e is the analytical value of the pressure, and where Gaussian quadrature was used to evaluate the integral associated with the functional. The predicted sensitivity of this functional to perturbations in y -momentum is depicted by the corresponding adjoint solution contours given in Figure 6 along with the initial computational mesh.

The refinement criteria adopted in the h -based AMR gradient-based approach applied to the Ringleb flow problem was based on the magnitude of the flow density gradient. The final meshes obtained using this

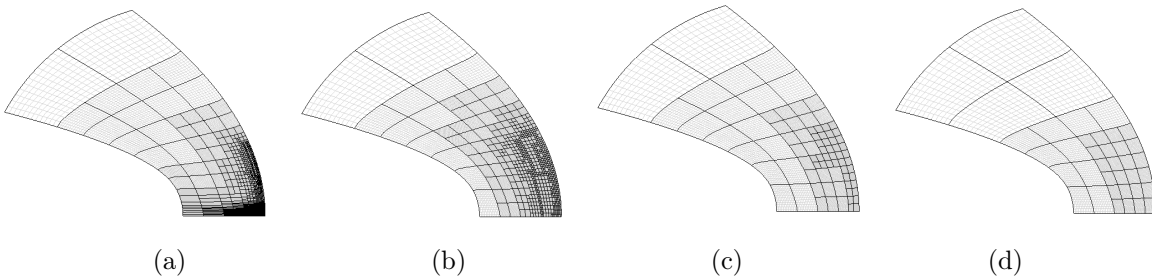


Figure 8: Select meshes obtained using output-based refinement strategies for various discretization orders, such that an equivalent actual error and error estimate is obtained.
(a) Using first-order CENO ($\mathcal{P} = 1$). After 9 refinements, the mesh has 1,182 blocks (680,832 cells), actual error of 1.73×10^0 , and error estimate of 3.54×10^{-1} .
(b) Using second-order CENO ($\mathcal{P} = 2$). After 5 refinements, the mesh has 710 blocks (408,960 cells), actual error of 2.34×10^{-4} , and error estimate of 2.01×10^{-5} .
(c) Using third-order CENO ($\mathcal{P} = 3$). After 3 refinements, the mesh has 80 blocks (46,080 cells), actual error of 4.62×10^{-4} , and error estimate of 2.15×10^{-4} .
(d) Using fourth-order CENO ($\mathcal{P} = 4$). After 2 refinements, the mesh has 38 blocks (21,888 cells), actual error of 2.37×10^{-5} , and error estimate of 1.70×10^{-5} .

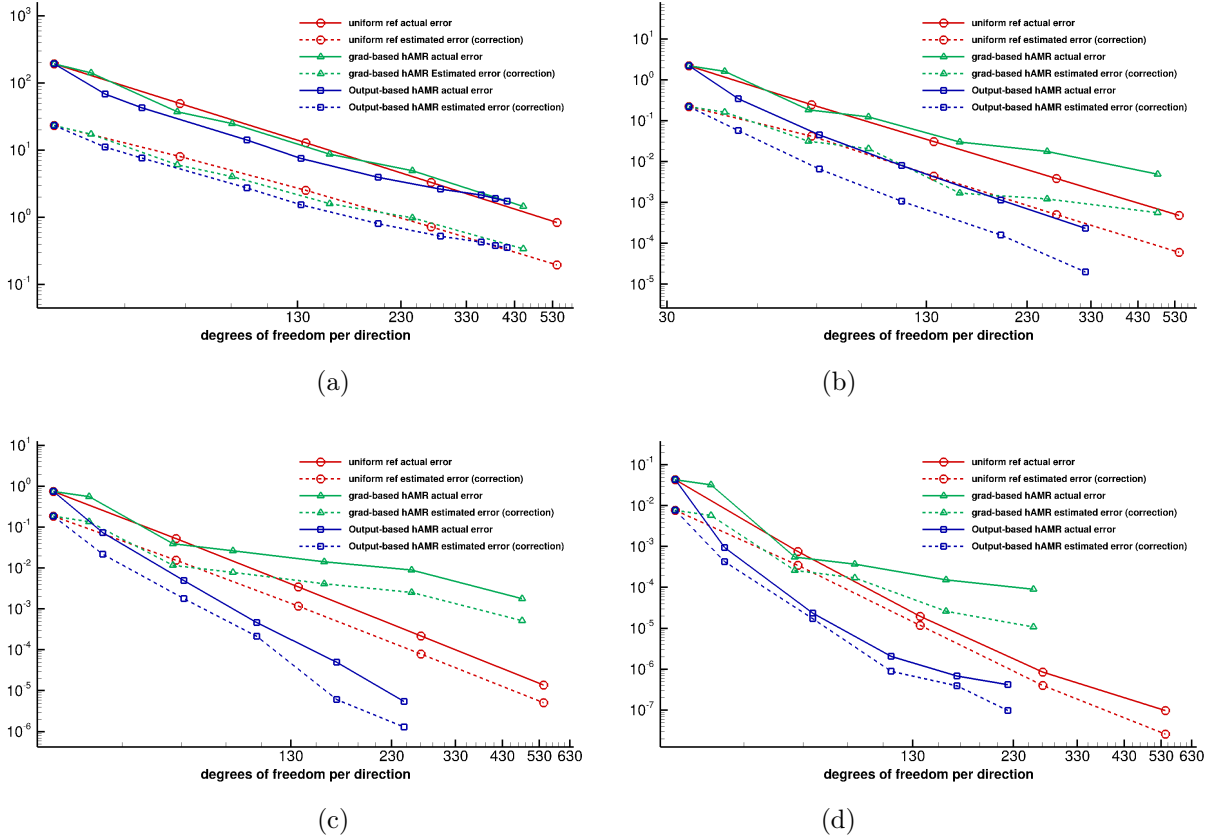


Figure 9: Functional convergence of pressure error and error estimate using uniform refinement, gradient-based and output-based refinement strategies for various discretization orders. (a) Using first-order CENO ($\mathcal{P} = 1$). (b) Using second-order CENO ($\mathcal{P} = 2$). (c) Using third-order CENO ($\mathcal{P} = 3$). (d) Using fourth-order CENO ($\mathcal{P} = 4$).

approach for various orders of \mathcal{P} are depicted in Figure 7. The convergence of the actual error and the error estimate is depicted in Figure 9 (a-d). It is evident that the application of gradient-based AMR does not yield significantly improved results when compared to straightforward uniform refinement of the mesh. As a matter of fact, the gradient-based approach would seem to perform worse than uniform refinement. This can be attributed to over-refinement of regions that do not contribute to improved functional accuracy. The meshes depicted in Figures 7 confirm this, where the bulk of refinement is focused in the vicinity of the sonic region adjacent to the inner streamline or left boundary.

Conversely, the output-based AMR approach was found to outperform both the uniform and gradient-based strategies. As can be seen in Figures 8(a-d), the regions marked for mesh refinement were those evaluated to have significant contribution to functional accuracy. In this case, these aforementioned regions were those in the vicinity of the right boundary. For an equivalent mesh count, the output-based approach achieves actual error and error estimates that are approximately two orders of magnitude lower than the gradient-based approach as shown in Figure 9.

6.3 Uniform and Adaptive p -Refinement

For a fixed mesh size, the effect of uniform p -refinement on the convergence of the actual error and error estimate can be obtained from the results shown in Figure 9. In addition, the proposed output-based scheme was then used to perform adaptive p refinement. The selected mesh size consisted of 32 blocks (18,432 cells) as shown in Figure 10(a), while the locally p -adapted blocks are indicated in Figure 10 (c).

For the uniform p refinement approach, as the value of \mathcal{P} increases, both the actual error and error

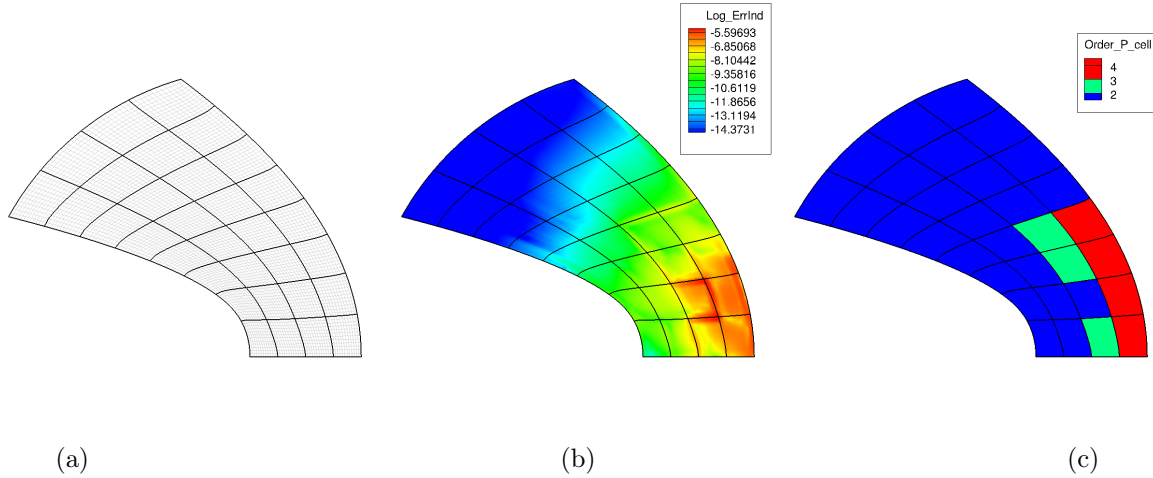


Figure 10: Selected contours for mesh with adaptive p -refinement.
 (a) fixed mesh of 32 blocks (18,432 cells).
 (b) error indicator highlighting regions contributing most to functional error.
 (c) local p -levels in blocks that were flagged for adaptive p -refinement.

estimates are of increasingly higher accuracy and display faster convergence rates. For example, given a mesh size of approximately 1.2 million cells (≈ 530 degrees of freedom per direction), fourth-order accurate CENO yields functional error and error estimates that are 7 orders of magnitude lower than the first-order accurate

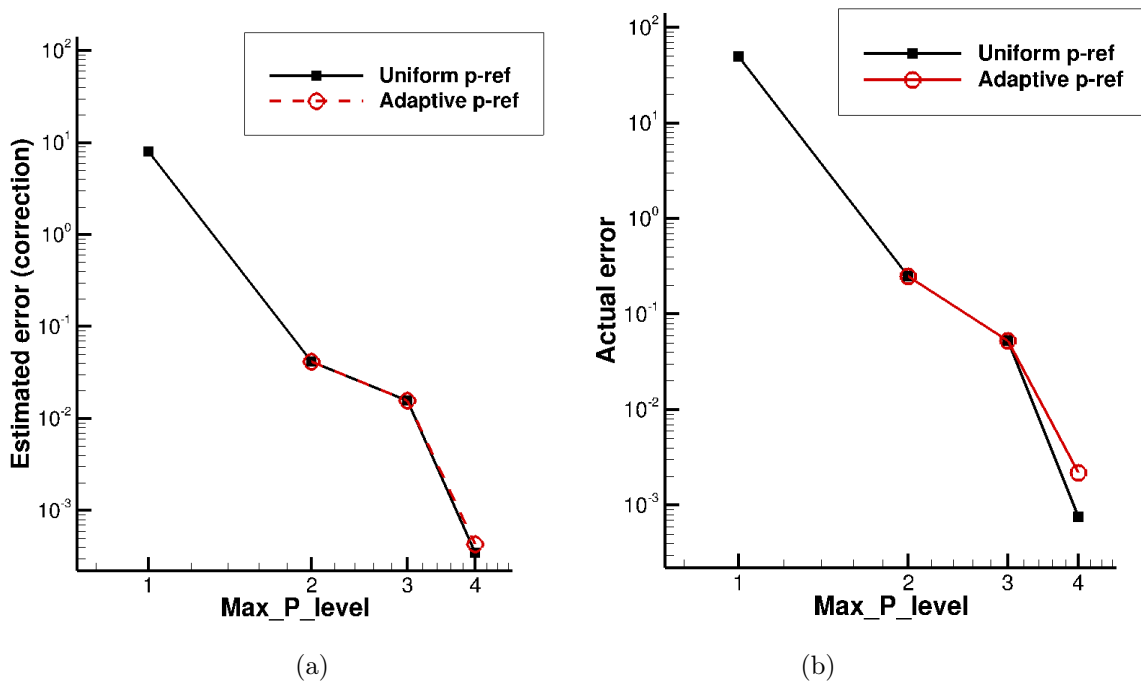


Figure 11: Convergence of error estimate and actual error using uniform p -refinement and adaptive p -refinement on a fixed mesh of 32 blocks (18,432 cells).

method. Another key benefit of order refinement that can be observed a lower mesh count is required to achieve a given level of functional accuracy. From this figure, it can be seen that using fourth-order CENO ($\mathcal{P} = 4$) uses 0.05 times a smaller mesh than second-order CENO ($\mathcal{P} = 2$) to achieve similar functional accuracy and error estimate. The adaptive p -refinement approach can be seen to result in errors that are fairly close to those obtained using a uniform p -refinement approach, as can be seen in the convergence results are shown in Figures 11 (a-b).

6.4 Adaptive h - p Refinement

Lastly, a combined h - p refinement strategy was then applied to the transonic Ringleb flow problem following the evaluation of the error convergence with uniform and adaptive p refinement. Starting with an underlying discretization of order $\mathcal{P} = 2$, the adjoint solution was computed to determine blocks to be flagged for refinement. Based on the smoothness indicator, flagged blocks deemed to have smooth solution were prescribed p -refinement, whereas those deemed to be non-smooth were set for h -refinement. Figure 12 highlights some selected computational grids showing \mathcal{P} levels and mesh refinement. Furthermore, the effect of h - p refine-

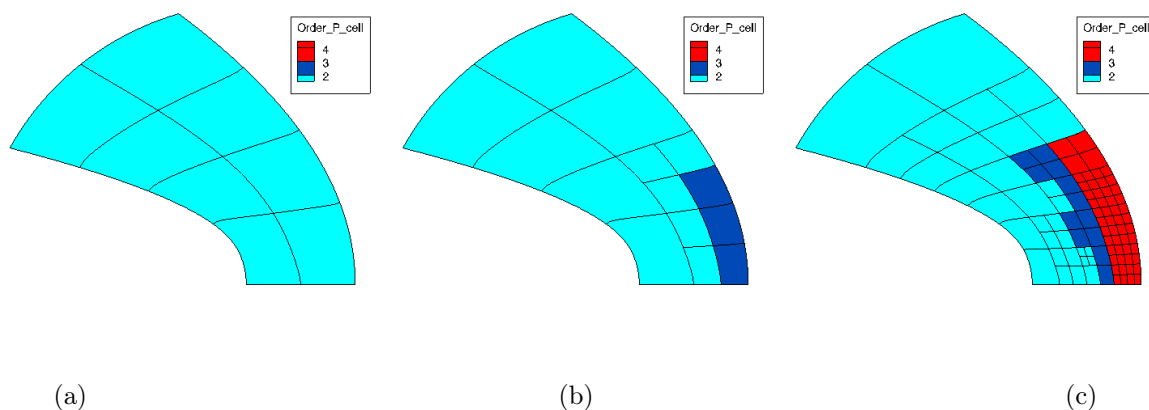


Figure 12: Selected grids showing the mesh and order refinement levels in hybrid h - p -refinement.

- (a) Initial block of 8 blocks (4,608 cells) at $\mathcal{P} = 2$.
- (b) Grid after 2 cycles of h - p refinement, resulting in 14 blocks (8,064 cells) and local values of $\mathcal{P} = \{2, 3\}$.
- (c) Grid after 5 cycles of h - p refinement, resulting in 95 blocks (96,192 cells) and local values of $\mathcal{P} = \{2, 3, 4\}$.

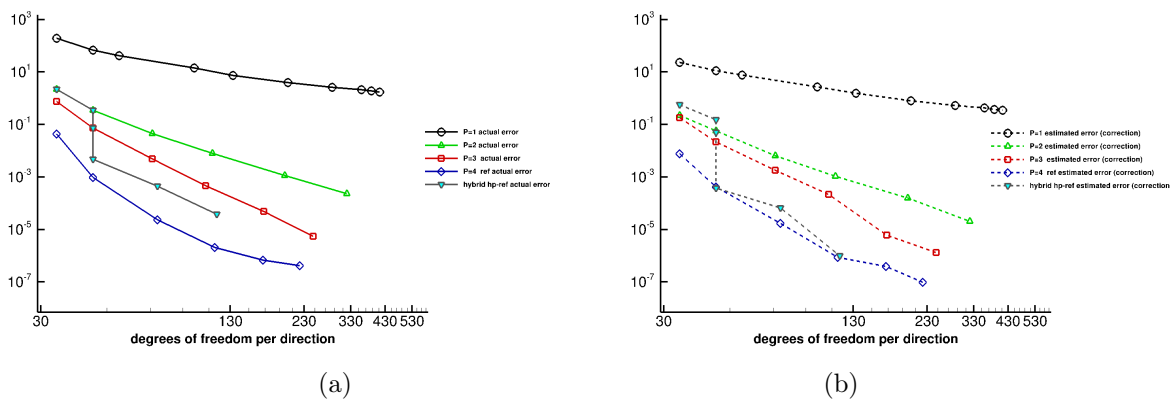


Figure 13: Comparison of adaptive h refinement and hybrid h - p refinement for convergence of (a) actual error and (b) error estimate for output-based technique.

ment can be compared to h refinement for various levels of P and this as depicted in Figure 13. From this figure, it was observed that h - p approach trends towards a convergence between $\mathcal{P} = 3$ and $\mathcal{P} = 4$.

7 Conclusions and Future Work

A novel hybrid h - p refinement technique method based on output-based error estimation has been considered and applied to the prediction of compressible inviscid gaseous flows governed by the Euler equations. The proposed h - p refinement strategy makes use of an anisotropic AMR valid for 3D, multi-block, body-fitted, hexahedral meshes, and is used in combination with a high-order CENO finite-volume scheme. An efficient Newton method is applied to obtain steady-state solutions to the governing equations on a given computational grid. Functional error estimates and p -derived refinement indicators are calculated to identify regions for increased solution accuracy. The solution smoothness indicator of the CENO scheme is used to select between h - and p -refinement, where local h -refinement is applied in non-smooth regions while local p -refinement is applied in smooth regions. Variants of the smoothness indicator are also used to direct the application of h refinement in an anisotropic manner.

The proposed output-based scheme has been applied to a transonic Ringleb flow problem for which there exists an analytical solution. For this Ringleb flow case, the standard gradient-based AMR strategy was shown not produce well converged estimates of the functional as the mesh refinement was focused on regions that did not significantly contribute to the accuracy of the functional. Of particular note was that uniform refinement yielded more suitable results compared to the gradient-based approach. The output-based error estimation for directing the AMR was found to offer performance benefits when compared to physics-based methods, even in the absence of discontinuities and sharp gradients. While the combined hybrid h - p algorithm was not fully explored, the use of mesh refinement in conjunction with varying orders of spatial discretization scheme was investigated. It was shown for the smooth case in consideration that use of a higher-order scheme resulted in more rapid functional convergence with corresponding lower error estimates. Moreover, the required mesh size for achieving a given level of accuracy was often much lower than that required by a lower-order discretization scheme. The effect of adaptive p -refinement was investigated and found to yield results similar to that of uniform p -refinement applied to the entire domain. Follow-on research will consider the application and evaluation of the proposed output-based error estimation and anisotropic AMR schemes with hybrid h - p refinement to a wider range of problems.

References

- [1] A. Harten, B. Enquist, S. Osher, and S. R. Chakravarthy. Uniformly high order accurate essentially non-oscillatory schemes, III. *J. Comput. Phys.*, 71:231–303, 1987.
- [2] Y. Sun, Z. J. Wang, and Y. Liu. High-order multidomain spectral difference methods for the Navier-Stokes equations. Paper 2006-0301, AIAA, January 2006.
- [3] G. May and A. Jameson. High-order accurate methods for high-speed flow. Paper 2005-5251, AIAA, June 2005.
- [4] G. May and A. Jameson. A spectral difference method for the Euler and Navier-Stokes equations on unstructured meshes. Paper 2006-304, AIAA, January 2006.
- [5] B. Cockburn and C.-W. Shu. TVB Runge-Kutta local projection discontinuous Galerkin finite-element method for conservation laws II: General framework. *Math. Comp.*, 52:411, 1989.
- [6] B. Cockburn, S.-Y. Lin, and C.-W. Shu. TVB Runge-Kutta local projection discontinuous Galerkin finite-element method for conservation laws III: One-dimensional systems. *J. Comput. Phys.*, 84:90, 1989.
- [7] B. Cockburn, S. Hou, and C.-W. Shu. TVB Runge-Kutta local projection discontinuous Galerkin finite-element method for conservation laws IV: The multidimensional case. *J. Comput. Phys.*, 54:545, 1990.
- [8] L. Ivan, H. De Sterck, S. A. Northrup, and C. P. T. Groth. Hyperbolic conservation laws on three-dimensional cubed-sphere grids: A parallel solution-adaptive simulation framework. *J. Comput. Phys.*, 255:205–227, 2013.
- [9] L. Ivan and C. P. T. Groth. High-order solution-adaptive central essentially non-oscillatory (CENO) method for viscous flows. *J. Comput. Phys.*, 257:830–862, 2014.

- [10] G.-S. Jiang and C.-W. Shu. Efficient implementation of weighted ENO schemes. *J. Comput. Phys.*, 126:202–228, 1996.
- [11] O. Friedrich. Weighted essentially non-oscillatory schemes for the interpolation of mean values on unstructured grids. *J. Comput. Phys.*, 144:194–212, 1998.
- [12] C. Hu and C.-W. Shu. Weighted essentially non-oscillatory schemes on triangular meshes. *J. Comput. Phys.*, 150:97–127, 1999.
- [13] L. Freret, C. P. T. Groth, T. B. Nguyen, and H. De Sterck. High-order finite-volume scheme with anisotropic adaptive mesh refinement: Efficient inexact Newton method for steady three-dimensional flows. Paper 2017-3297, AIAA, June 2017.
- [14] T. J. Barth. Recent developments in high order k-exact reconstruction on unstructured meshes. Paper 93-0668, AIAA, January 1993.
- [15] M. J. Berger. *Adaptive Mesh Refinement for Hyperbolic Partial Differential Equations*. PhD thesis, Stanford University, January 1982.
- [16] M. J. Berger and J. Olinger. Adaptive mesh refinement for hyperbolic partial differential equations. *J. Comput. Phys.*, 53:484–512, 1984.
- [17] M. J. Berger. Data structures for adaptive grid generation. *SIAM J. Sci. Stat. Comput.*, 7(3):904–916, 1986.
- [18] M. J. Aftosmis, M. J. Berger, and G. Adomavicius. A parallel multilevel method for adaptively refined Cartesian grids with embedded boundaries. Paper 2000-0808, AIAA, January 2000.
- [19] X. Gao and C. P. T. Groth. A parallel solution-adaptive method for three-dimensional turbulent non-premixed combustions flows. *J. Comput. Phys.*, 229(5):3250–3275, 2010.
- [20] S. A. Northrup. *A Parallel Implicit Adaptive Mesh Refinement Algorithm for Predicting Unsteady Fully-Compressible Reactive Flows*. PhD thesis, University of Toronto, December 2013.
- [21] M. R. J. Charest, C. P. T. Groth, and Ö. L. Gülder. Numerical study on the effect of gravity on flame shape and radiation in laminar diffusion flames. In *Proceedings of the Combustion Institute Canadian Section Spring Technical Meeting*, pages 84–89, Toronto, Canada, May 12–14 2008.
- [22] L. Freret and C. P. T. Groth. Anisotropic non-uniform block-based adaptive mesh refinement for three-dimensional inviscid and viscous flows. Paper 2015-2613, AIAA, June 2015.
- [23] L. Freret, L. Ivan, H. De Sterck, and C. P. T. Groth. High-order finite-volume method with block-based AMR for magnetohydrodynamics flows. *J. Sci. Comput.*, 79(1):176–208, 2019.
- [24] C. P. T. Groth, D. L. De Zeeuw, K. G. Powell, T. I. Gombosi, and Q. F. Stout. A Parallel Solution-Adaptive Scheme for Ideal Magnetohydrodynamics. Paper 99-3273, AIAA, June 1999.
- [25] L. Ivan. *Development of High-Order CENO Finite-Volume Schemes with Block-Based Adaptive Mesh Refinement*. PhD thesis, University of Toronto, August 2011.
- [26] M. J. Williamschen and C. P. T. Groth. Parallel anisotropic block-based adaptive mesh refinement algorithm for three-dimensional flows. Paper 2013-2442, AIAA, June 2013.
- [27] Z. J. Zhang and C. P. T. Groth. Parallel high-order anisotropic block-based adaptive mesh refinement finite-volume scheme. Paper 2011-3695, AIAA, June 2011.
- [28] L. Freret and C. P. T. Groth. Anisotropic Non-Uniform Block-Based Adaptive Mesh Refinement for Three-Dimensional Inviscid and Viscous Flows. Paper 2015-2613, American Institute of Aeronautics and Astronautics, June 2015.
- [29] S. A. Northrup and C. P. T. Groth. Solution of laminar diffusion flames using a parallel adaptive mesh refinement algorithm. Paper 2005-0547, AIAA, January 2005.
- [30] L. Freret, L. Ivan, H. De Sterck, and C. P. T. Groth. A high-order finite-volume method with anisotropic AMR for ideal MHD flows. Paper 2017-0845, AIAA, January 2017.
- [31] M. B. Giles and N. A. Pierce. An introduction to the adjoint approach to design. *Flow Turb. Combust.*, 65:393–415, 2000.
- [32] L. Freret, C. N. Ngigi, T.B. Nguyen, H. De Sterck, and C.P.T. Groth. High-order finite-volume scheme with anisotropic adaptive mesh refinement: Efficient inexact newton method for steady three-dimensional flows. 2022.
- [33] R. Becker and R. Rannacher. Weighted A Posteriori Error Control in Finite Element Methods. Technical report, preprint No. 96-1, Universitat Heidelberg, 1994.
- [34] D. A. Venditti and D. L. Darmofal. Adjoint error estimation and grid adaptation for functional outputs: Application to quasi-one-dimensional flow. *J. Comput. Phys.*, 164:204–227, 2000.

- [35] M. Nemeć and M. J. Aftosmis. Adjoint error estimation and adaptive refinement for embedded-boundary Cartesian meshes. Paper 2007-4187, AIAA, June 2007.
- [36] I. Babuska and B. Szabo. On the rates of convergence of the finite element method. *Int. J. Numer. Meth. Engin.*, 18:323–341, 1982.
- [37] J. T. Oden, L. Demkowicz, W. Rachowicz, and T. A. Westermann. Toward a universal hp adaptive finite element strategy, part 2. a posteriori error estimation. *Comp. Meth. Appl. Mech. Engrg.*, 77:113–180, 1989.
- [38] L. Demkowicz, W. Rachowicz, and P. Devloo. A fully automatic hp-adaptivity. *J. Sci. Comput.*, 17:117–142, 2002.
- [39] V. Dolejsi. Anisotropic hp-adaptive method based on interpolation error estimates in the lq-norm. *Appl. Numer. Math.*, 82:80–114, 2014.
- [40] V. Dolejsi, G. May, and A. Rangarajan. A continuous hp-mesh model for adaptive discontinuous galerkin schemes. *Appl. Numer. Math.*, 124:1–24, 2018.
- [41] A. Jalali and C. Ollivier-Gooch. An hp-adaptive unstructured finite volume solver for compressible flows. *Int. J. Numer. Meth. Fluids*, 85:563–582, 2017.
- [42] O. Zienkiewicz, R. Taylor, and J.Z. Zhu. *Basic Concepts in the Finite Difference and Finite Element Methods*. Butterworth-Heinemann, 2013.
- [43] L. Lapidus and G. F. Pinder. *Basic Concepts in the Finite Difference and Finite Element Methods*. Wiley, 1999.
- [44] D. A. Venditti and D. L. Darmofal. Anisotropic grid adaptation for functional outputs: Application to two-dimensional viscous flows. *J. Comput. Phys.*, 187:22–46, 2003.
- [45] D. A. Venditti and D. L. Darmofal. Grid adaptation for functional outputs: Application to two-dimensional inviscid flows. *J. Comput. Phys.*, 176:40–69, 2002.
- [46] N. Narechania, L. Freret, and C. P. T. Groth. Block-based anisotropic amr with *a posteriori* adjoint-based error estimation for three-dimensional inviscid and viscous flows. Paper, AIAA, June 2017.
- [47] C. N. Ngigi, L. Freret, and C. P. T. Groth. Comparison of *h*- and *p*-derived output-based error estimates for directing anisotropic adaptive mesh refinement in three-dimensional inviscid flows. Paper, AIAA, January 2018.
- [48] M. Yano and D. L. Darmofal. An optimization framework for anisotropic simplex mesh adaptation. *J. Comput. Phys.*, 231:7626–7649, 2012.
- [49] M. A. Ceze and K. J. Fidkowski. An anisotropic *hp*-adaptation framework for functional prediction. *AIAA J.*, 51(2):492–509, 2013.
- [50] M. Wopen, A. Balan, G. May, and J. Schütz. A comparison of hybridized and standard DG methods for target-based *hp*-adaptive simulation of compressible flow. *Comp. Fluids*, 98:3–16, 2014.
- [51] B. Einfeldt. On Godunov-type methods for gas dynamics. *SIAM J. Numer. Anal.*, 25:294–318, 1988.
- [52] CPT Groth and SA Northrup. Parallel implicit adaptive mesh refinement scheme for body-fitted multi-block mesh. In *17th AIAA Computational Fluid Dynamics Conference, Toronto, Ontario, Canada, AIAA paper*, volume 5333, page 2005, 2005.
- [53] M.R.J. Charest, C.P.T. Groth, and Ö.L. Gülder. Solution of the equation of radiative transfer using a newton-krylov approach and adaptive mesh refinement. *J. Comput. Phys.*, 231(8):3023–3040, 2012.
- [54] Y. Saad and M.H. Schultz. Gmres: a generalized minimal residual algorithm for solving nonsymmetric linear systems. *SIAM J. Sci. Stat. Comput.*, 7(3):856–869, 1986.
- [55] L. Ivan, H. De Sterck, Northrup S., and C. Groth. Multi-dimensional finite-volume scheme for hyperbolic conservation laws on three-dimensional solution-adaptive cubed-sphere grids. *Journal of Computational Physics*, 255:205–227, 2013.
- [56] A. Harten, B. Enquist, S. Osher, and S. R. Chakravarthy. Uniformly high order accurate essentially non-oscillatory schemes, III. Report 86-22, ICASE, April 1986.
- [57] T. J. Barth and P. O. Fredrickson. Higher order solution of the Euler equations on unstructured grids using quadratic reconstruction. Paper 90-0013, AIAA, January 1990.
- [58] L. Ivan, H. De Sterck, A. Susanto, and C. Groth. High-order central eno finite-volume scheme for hyperbolic conservation laws on three-dimensional cubed-sphere grids. *Journal of Computational Physics*, 282:157–182, 2015.
- [59] V. Venkatakrisnan. On the accuracy of limiters and convergence to steady state solutions. Paper 93-0880, AIAA, January 1993.

- [60] A. Nejat and C. Ollivier-Gooch. A high-order accurate unstructured finite-volume Newton-Krylov algorithm for inviscid compressible flows. *J. Comput. Phys.*, 227:2582–2609, 2008.
- [61] A. Jalali. *An Adaptive Higher-order Unstructured Finite Volume Solver for Turbulent Compressible Flows*. PhD thesis, University of British Columbia, 2017.
- [62] S. Clain R. Costa, J. M. Nóbrega and G. J. Machado. Very high-order accurate polygonal mesh finite volume scheme for conjugate heat transfer problems with curved interfaces and imperfect contacts. *Computer Methods in Applied Mechanics and Engineering*, 117(2), 2019.
- [63] J. S. Sachdev, C. P. T. Groth, and J. J. Gottlieb. A parallel solution-adaptive scheme for predicting multi-phase core flows in solid propellant rocket motors. *Int. J. Comput. Fluid Dyn.*, 19(2):159–177, 2005.
- [64] X. Gao, S. A. Northrup, and C. P. T. Groth. Parallel solution-adaptive method for two-dimensional non-premixed combusting flows. *Prog. Comput. Fluid Dyn.*, 11(2):76–95, 2011.
- [65] X. Gao and C. P. T. Groth. A parallel adaptive mesh refinement algorithm for predicting turbulent non-premixed combusting flows. *Int. J. Comput. Fluid Dyn.*, 20(5):349–357, 2006.
- [66] X. Gao and C. P. T. Groth. A parallel solution-adaptive method for three-dimensional turbulent non-premixed combusting flows. *J. Comput. Phys.*, 229(5):3250–3275, 2010.
- [67] R. J. Hogan. Fast reverse-mode automatic differentiation using expression templates in c++. *ACM Trans. Math. Softw.*, 40:26:1–26:16, 2014.
- [68] M. Heroux, R. Bartlett, V. Howle, R. Hoekstra, J. Hu, T. Kolda, R. Lehoucq, K. Long, R. Pawlowski, E. Phipps, A. Salinger, H. Thornquist, R. Tuminaro, J. Willenbring, and A. Williams. An Overview of Trilinos. Technical Report SAND2003-2927, Sandia National Laboratories, 2003.
- [69] D. A. Venditti and D. L. Darmofal. Anisotropic grid adaptation for functional outputs: Application to two-dimensional viscous flows. *J. Comput. Phys.*, 187:22–46, 2003.
- [70] R. Becker and R. Rannacher. An optimal control approach to a posteriori error estimation in finite element methods. *Acta Num.*, 10:1–102, 2001.
- [71] L. Ivan and C. P. T. Groth. High-order central ENO finite-volume scheme with adaptive mesh refinement. Paper 2007-4324, AIAA, June 2007.
- [72] M. Yano, J. Modisette, and D. Darmofal. The importance of mesh adaptation for higher-order discretizations of aerodynamic flows. Paper 2011-3852, AIAA, June 2011.
- [73] M. A. Ceze and K. J. Fidkowski. An anisotropic hp-adaptation framework for functional prediction. *American Institute of Aeronautics and Astronautics Journal*, 51:492–509, 2013.
- [74] J. Peraire, M. Vahdati, K. Morgan, and O. G. Zienkiewicz. Adaptive remeshing for compressible flow computations. *J. Comput. Phys.*, 72:449–466, 1987.
- [75] K. J. Fidkowski. *A Simplex Cut-Cell Adaptive Method for High-Order Discretizations of the Compressible Navier-Stokes Equations*. PhD thesis, Massachusetts Institute of Technology, 2007.
- [76] AGARD Subcommittee C. Test cases for inviscid flow field methods. Advisory Report 211, AGARD, 1986.
- [77] W. J. Coirier and K. G. Powell. An accuracy assessment of Cartesian-mesh approaches for the Euler equations. *J. Comput. Phys.*, 117:121–131, 1995.